

# RADIATION-HYDRODYNAMICAL MODELLING OF CORE-COLLAPSE SUPERNOVAE: LIGHT CURVES AND THE EVOLUTION OF PHOTOSPHERIC VELOCITY AND TEMPERATURE

M. L. PUMO<sup>1,2,3</sup> & L. ZAMPIERI<sup>1</sup>

<sup>1</sup>INAF-Osservatorio Astronomico di Padova, Vicolo dell'Osservatorio 5, I-35122 Padova, Italy

<sup>2</sup>Bonino-Pulejo Foundation, Via Uberto Bonino 15/C, I-98124 Messina, Italy and

<sup>3</sup>INAF-Osservatorio Astrofisico di Catania, via S. Sofia 78, I-95123 Catania, Italy

(Dated: Received ... ; accepted ...)

*Draft version August 4, 2011*

## ABSTRACT

We have developed a relativistic, radiation-hydrodynamics Lagrangian code, specifically tailored to simulate the evolution of the main observables (light curve, evolution of photospheric velocity and temperature) in core-collapse supernova (CC-SN) events. The distinctive features of the code are an accurate treatment of radiative transfer coupled to relativistic hydrodynamics, a self-consistent treatment of the evolution of the innermost ejecta taking into account the gravitational effects of the central compact remnant, and a fully implicit Lagrangian approach to the solution of the coupled non-linear finite difference system of equations. Our aim is to use it as numerical tool to perform calculations of grid of models to be compared with observation of CC-SNe. In this paper we present some testcase simulations and a comparison with observations of SN 1987A, as well as with the results obtained with other numerical codes. We also briefly discuss the influence of the main physical parameters (ejected mass, progenitor radius, explosion energy, amount of <sup>56</sup>Ni) on the evolution of the ejecta, and the implications of our results in connection with the possibility to “standardize” hydrogen-rich CC-SNe for using them as candles to measure cosmological distances.

*Subject headings:* supernovae: general — hydrodynamics — radiative transfer — methods: numerical — supernovae: individual (SN 1987A) — distance scale

## 1. INTRODUCTION

It is widely accepted that core-collapse supernovae (CC-SNe) represent the final explosive evolutionary phase of stars having initial (i.e. main sequence) masses larger than  $\sim 8\text{--}10M_{\odot}$  (e.g. Woosley & Weaver 1986; Hamuy 2003a; Heger et al. 2003). As such, CC-SNe are fundamental probes of the stellar evolution of massive stars and can be used to understand the link among explosion mechanism, nature of remnants, progenitors evolution, and environment around progenitors (e.g. Filippenko 1997; Cappellaro & Turatto 2000).

In addition to their intrinsic interest, CC-SNe are relevant to many astrophysical issues. For example, the CC-SNe influence the physical evolution of galaxies, their frequency being related to the ongoing star formation rate (e.g. Cappellaro et al. 2005; Madau, Della Valle, & Panagia 1998) and determining the kinematics and the structure of the interstellar medium (e.g. Ratnatunga & van den Bergh 1989). CC-SNe are also important because of their role in the production of neutrinos, cosmic rays and, probably, gravitational waves (e.g. Haungs, Rebel, & Roth 2003; Duan & Kneller 2009; Pagliaroli et al. 2009). Additionally, the CC-SN ejecta, enriched in heavy elements, make CC-SNe key actors in the nucleosynthesis processes of intermediate and trans-iron elements and in the chemical evolution of galaxies (e.g. Arnett 1996; Chieffi, Limongi, & Straniero 1998). Moreover, they seem to be particularly promising to measure cosmological distances in addition to type Ia SNe (e.g. Nugent et al. 2006; Zampieri 2007; Olivares et al. 2010, and references therein).

In spite of the importance of these explosive events

in astrophysics, there are still basic questions to be answered on CC-SNe, related to the extreme variety of their displays. Indeed they appear to show different energetics and to eject rather diverse amounts of material, causing rather heterogeneous behaviors of their light curves and spectra (e.g. Turatto, Benetti, & Pastorello 2007). This apparent heterogeneity may be linked to stellar evolution effects and to the explosion mechanism (e.g. Pumo et al. 2009, and references therein), but the exact link between the physical properties of the explosion (ejected mass, explosion energy, stellar structure and composition at the explosion) and the observational characteristics is far from being well-established.

Light curve and spectral modelling have often successfully been used to provide information about the physical properties of single CC-SNe (e.g. SNe 1987A, 1993J, 1999em, 2004et, and 2005cs; see Shigeyama, Nomoto, & Hashimoto 1988; Woosley 1988; Shigeyama & Nomoto 1990; Blinnikov et al. 1998; Utrobin 2004, 2007; Baklanov, Blinnikov, & Pavlyuk 2005; Utrobin & Chugai 2008; Pastorello et al. 2009; Bersten, Benvenuto, & Hamuy 2011). Comparatively little effort has been devoted to investigating large samples of these events and trying to explain the significant range of properties that they show. Differences in luminosity, expansion velocity and <sup>56</sup>Ni yields are very large (up to  $\sim 2$  order of magnitude), and difficult to relate to changes in a single parameter, such as the mass of the progenitor star. However, despite this, variations in the observed properties appear to obey a certain order. Some correlations among different observables have been noted (e.g. Hamuy 2003b; Zampieri 2007) and used to calibrate CC-SNe as distance indicators (e.g.

Hamuy & Pinto 2002; Hamuy 2003b; Nugent et al. 2006; Olivares et al. 2010), in addition to Baade-Wessellink type, spectral based techniques (like the expanding photosphere method, see e.g. Kirshner & Kwan 1974; Eastman, Schmidt, & Kirshner 1996; Dessart et al. 2008; or the spectral-fitting expanding atmosphere method, see e.g. Mitchell et al. 2002; Baron et al. 2004).

While parameter studies of the light curves of CC-SNe have been largely pursued in the past both with analytical (e.g. Blinnikov & Popov 1993; Popov 1993; Arnett 1996, and references therein) and numerical (e.g. Litvinova & Nadezhin 1983, 1985; Young 2004; Dessart, Livne, & Waldman 2010) techniques, only a few systematic theoretical investigations of the physical origin of the aforementioned correlations have been performed (e.g. Zampieri 2007; Kasen & Woosley 2009). It is still not completely clear how variations of basic parameters conspire in such a way to give rise to the observed relations. In particular, Kasen & Woosley (2009) found that the relation between luminosity and expansion velocity at 50 days is explained by the behavior of hydrogen recombination in the SN envelope and proposed additional correlations based only on photometric data. A better physical understanding of these correlations would allow us, on one side, to pinpoint possible biases that may affect the use of CC-SNe as standard candles and, on the other side, to look for other correlations that may reveal more promising when applied to high redshift SNe.

With the aim of clarifying the aforementioned astrophysical issues, we have improved on previous work that we started on the numerical modelling of SN ejecta and fallback (Zampieri et al. 1998; Balberg, Zampieri, & Shapiro 2000), and on the physical interpretation of the heterogeneous behavior of Type II plateau SNe (Zampieri et al. 2003; Zampieri 2005, 2007). In this paper we present a new, improved version of a general-relativistic, radiation hydrodynamics, Lagrangian code tailored to the modelling of CC-SNe. Similar numerical treatment of the expanding SN envelope have been presented in the literature (e.g. Blinnikov et al. 1998; Iwamoto et al. 2000; Chieffi et al. 2003; Young 2004; Kasen & Woosley 2009; Bersten et al. 2011). Our code has the advantage of being able to follow the fallback of material on the central remnant in a fully relativistic formalism, and allows for an accurate treatment of radiative transfer in all regimes. It will enable us to explore the physical behavior of CC-SNe, to link their physical and observational properties, to investigate the existence of correlations among their different observables, and also to perform model fitting of single events.

The plan of the paper is the following. In sect. 2 we describe the features of the new version of the code (details on the adopted numerical procedure and on the finite difference form of the equations are presented in the Appendix). Sect. 3 illustrates the numerical calculations. Sect. 4 is devoted to the code validation and the analysis of the basic physical properties of the ejecta in presence of a central compact remnant during all the different evolutionary stages. A summary with final comments and a short discussion of the implications of our results in connection with the possibility to “standardize” hydrogen-rich CC-SNe is presented in Sect. 5.

## 2. CODE DESCRIPTION

The code is a new, improved version of a general-relativistic, radiation hydrodynamics, Lagrangian code described in Zampieri, Miller, & Turolla (1996), Zampieri et al. (1998) and in Balberg et al. (2000), and originally developed for studying spherical accretion onto black holes and fall back in the aftermath of a SN explosion.

This new version of the code is able to compute the evolution of the ejecta and the emitted luminosity, from the breakout of the shock wave at the stellar surface up to the nebular stage (when the envelope has recombined and the energy budget is dominated by the radioactive decays of the heavy elements synthesized in the explosion). We solve the equations of relativistic radiation hydrodynamics in spherical symmetry for a self-gravitating matter fluid which interacts with radiation, taking into account the heating effects due to decays of radioactive isotopes synthesized in the SN explosion. The distinctive features of the code are summarized here, while a detailed description of the equations, numerical method and input physics is reported below (see sections 2.1 through 2.4). The code encompasses:

- an accurate treatment of radiative transfer in all regimes from the one in which the ejecta are optically thick up to when they are completely transparent. This is obtained through the solution of the first two moments of the radiative transfer equations (Eqs. [2] and [3] in sect. 2.1). Although it is necessary to adopt a closure relation, which is constrained only in the asymptotic optically thick/thin regimes (see Zampieri et al. 1996, 1998, for more details), the uncertainty induced by this approximation is not significant for wavelength(frequency)-integrated radiative transfer (see e.g. Nobili & Turolla 1988) and this approach is definitely superior to any treatment based on the diffusion approximation;
- the coupling of the radiation moment equations with the equations of relativistic hydrodynamics, adopting a fully implicit Lagrangian finite difference scheme (see sect. 2.1 and 2.2 for details);
- the possibility to compute the evolution of the ejecta and the emitted luminosity taking into account the gravitational effects of the compact remnant. This enables the code to deal with the fallback of material onto the compact remnant and, consequently, to accurately determining the amount of ejected  $^{56}\text{Ni}$ .

The main limitation of our code compared to other similar codes (e.g. Young 2004, Kasen & Woosley 2009, and Dessart, Livne, & Waldman 2010) is that we consider only wavelength integrated radiation energy density and luminosity, and hence we cannot compute the actual spectrum of the SN. Also, the evolution starts from “ad hoc” initial conditions that mimic the profiles of the physical variables after shock and reverse shock passage, but such conditions are not meant to be “perfectly realistic”, in the sense to be the outcome of a stellar evolution code coupled with numerical computations of the explosion phase. Some improvements in this respect have been

already added to the present version of the code (see sect. 2.3 for details). At the same time, we are working (in collaboration with A. Chieffi and M. Limongi) at interfacing it with the output of a hydrodynamical code that follows the CC-SN explosion and the explosive nucleosynthesis, starting from pre-SN models obtained through a stellar evolutionary code.

### 2.1. Equations

Since we consider the effects of the central compact remnant on the evolution of the ejecta, we adopt a fully general relativistic treatment. The equations governing the relativistic radiation hydrodynamics of the expanding ejecta in spherically symmetry are reported in Zampieri et al. (1996, 1998) and Balberg et al. (2000). The main physical variables that describe the behavior of the ejecta are the gas mass density  $\rho$ , and the gas internal energy per unit mass  $\epsilon$  and pressure  $p$  (measured in the frame comoving with the ejecta). Those describing the radiation field are the radiation energy density  $w_0$  and flux  $w_1$  (both in units of  $\text{erg cm}^{-3}$ ). We refer to Zampieri et al. (1998) for the full set of equations and related quantities, while here we summarize for convenience the gas energy equation and the first two moments of the radiative transfer equations, whose treatment has been deeply modified in the present analysis. They read:

$$\epsilon_{,t} + ak_P(B - w_0) + p \left( \frac{1}{\rho} \right)_{,t} = Q \quad \text{energy eq.,} \quad (1)$$

$$(w_0)_{,t} - ak_P \rho (B - w_0) + w_0 \left[ \frac{4}{3} \left( \frac{b_{,t}}{b} + 2 \frac{r_{,t}}{r} \right) + f \left( \frac{b_{,t}}{b} - \frac{r_{,t}}{r} \right) \right] + \frac{1}{abr^2} (w_1 a^2 r^2)_{,\mu} = 0 \quad \text{zero-th moment eq.,} \quad (2)$$

$$(w_1)_{,t} + ak_R \rho w_1 + 2w_1 \left( \frac{b_{,t}}{b} + \frac{r_{,t}}{r} \right) + a \left[ \frac{1}{3a^4 b} (w_0 a^4)_{,\mu} + \frac{1}{3br^3} (f w_0 a r^3)_{,\mu} \right] = 0 \quad \text{first moment eq.,} \quad (3)$$

where  $t$  and  $\mu$  are the Lagrangian time and mass contained within a comoving spherical shell of radius  $r$  (a comma denotes partial derivatives with respect to the corresponding variable),  $a$  (00 metric coefficient) is a function of  $t$  and  $\mu$  (computed from Eq. [6] in Zampieri et al. 1998),  $b = 1/(4\pi r^2 \rho)$ ,  $B = a_R T^4$  ( $a_R$  blackbody radiation constant),  $Q$  is the heating rate of radioactive decays from the isotopes synthesized in the SN explosion (see sect. 2.4), and  $k_P$  and  $k_R$  are Planck mean and Rosseland mean opacity, respectively. The dependence on the gas temperature  $T$  is contained in  $\epsilon$ ,  $p$ ,  $k_P$  and  $k_R$ , and is specified through the equations of state (see sect. 2.4).  $k_P$  and  $k_R$  are calculated interpolating the TOPS opacities as a function of  $T$  and  $\rho$  (see again sect. 2.4). Finally, the function  $f$  (Eddington factor), relating the second-order moment of the radiation intensity to  $w_0$ , is calculated using Eqs. [12] and [13] in Zampieri et al. (1998).

### 2.2. Numerical method

In order to solve the complete system of equations of relativistic radiation hydrodynamics, the old version of the code adopts a semi-implicit Lagrangian finite difference scheme where the time step is controlled by the Courant condition and the requirement that the fractional variation of the variables in one time-step be smaller than 10%. The energy equation (Eq. [1]) and the zero-th moment of the radiative transfer equation (Eq. [2]) form a non-linear system of equations in the gas temperature  $T$  and are then solved point-by-point on the computational grid using a Newton-Raphson iterative method (see the Appendix in Zampieri et al. 1998, for details).

We have deeply modified the numerical treatment previously adopted by implementing a fully implicit Lagrangian finite difference scheme. This allows for a major improvement in the numerical stability and overall computational efficiency of the code, especially during those phases when fast motions of steep gradients occur (e.g. the radiative recombination phase). The first moment equation for the radiative flux  $w_1$  (Eq. [3]) is now solved together with Eqs. [1] and [2] in a fully implicit scheme on the whole computational grid, that requires a modification of the temporal centering of the variables. This leads to a highly non-linear system of equations that is solved through a Newton-Raphson iterative method and matrix inversion packages that minimise the CPU time and the required storage space. In the Appendix we report more details on the finite difference form of the Eqs. [1], [2] and [3], and the numerical procedure adopted to solve them.

### 2.3. Initial and boundary conditions

In the present analysis we consider the evolution of the ejecta after the explosion phase<sup>1</sup>. At this stage, the SN shock wave has already propagated through the envelope of the progenitor star redistributing the explosion energy through it, and the evolution starts when the envelope is essentially free-coasting and in homologous expansion. We assume that it is comprised of a mixture of hydrogen, helium and heavier elements. As oxygen is expected to be the most abundant heavy element, we further assume that it represents the entire metal component in the envelope's final composition (see Balberg et al. 2000). The mass fraction of  $^{56}\text{Ni}$  is assumed to be concentrated towards the center and to vary as a function of Lagrangian mass  $\mu$  as:

$$X_{^{56}\text{Ni}}(\mu) = X_{^{56}\text{Ni},0} \times \exp \left[ -K_{mix} \frac{\mu}{\mu_{max}} \right], \quad (4)$$

where  $X_{^{56}\text{Ni},0}$  is the initial mass fraction of  $^{56}\text{Ni}$  at the inner boundary of the ejecta,  $K_{mix}$  is a numerical constant whose value is essentially related to the extent of mixing

<sup>1</sup> We are working at interfacing our code with the output of self-consistent calculations of the explosion phase, but during this testing phase we preferred to assume idealized initial conditions that provide an approximate description of the ejected material after shock (and possible reverse shock) passage. Clearly, as the actual velocity, density and heavy element distributions of the post-shock material may affect the light curve and the determination of the envelope's physical parameters in a significant way, at present we can provide only approximate estimates of these quantities.

of  $^{56}\text{Ni}$  throughout the envelope, and  $\mu_{max}$  is the value of  $\mu$  at the outer boundary, equal to the total envelope mass (see Appendix A for details).

Assuming that, at the onset of expansion, radiation is in local thermodynamic equilibrium (LTE hereafter) with the gas throughout the envelope and the initial photon mean free path  $\lambda_0$  is much smaller than the radius of the envelope, the initial temperature profile in the ejecta can be well approximated by the so-called “radiative zero solution” of Arnett (1980):

$$T(r(\mu), t = 0) = T_0 \times \left[ \frac{\sin(\pi x)}{\pi x} \right]^{\frac{1}{4}}, \quad (5)$$

where  $T_0$  is the initial central temperature,  $x = r/R_0$  and  $R_0 \equiv r(\mu_{max})$  is the initial radius of the outermost shell of the ejecta.

As the gas is initially in LTE with radiation, we assume that a polytropic relation with index  $\Gamma = 4/3$  holds. For a radiation dominated flow,  $P = a_R T^4/3 = K \rho^{4/3}$  ( $K$  polytropic constant) and hence

$$\rho(r(\mu), t = 0) = \rho_0 \times \left[ \frac{\sin(\pi x)}{\pi x} \right]^{\frac{3}{4}}, \quad (6)$$

with  $\rho_0 = (a_R/3K)^{3/4} T_0^3$ .

Considering that the envelope is expanding homologically, the initial velocity profile is given by:

$$v(r(\mu), t = 0) = V_0 \times \frac{r(\mu)}{R_0}, \quad (7)$$

where  $V_0$  is the initial velocity at the outer radial boundary  $R_0$ .

As for the radiation field, in the aforementioned assumptions the diffusion approximation holds. Therefore,  $w_0 = a_R T^4$  and  $w_1 \approx w_0/(k_R \rho r)$ , where  $k_R$  is approximated with the electron scattering opacity  $k_{es}$  (see Nobili, Turolla & Zampieri 1991).

For a fixed composition and radial distribution of  $^{56}\text{Ni}$ , four input parameters determine uniquely the dynamical and thermal properties of the expanding CC-SN envelope (including its initial kinetic and thermal energy): the total mass  $M_{env}$ , the initial radius  $R_0$ , the initial sound speed at the inner boundary  $c_{s0}$ , and the ratio  $\tilde{k}$  of the initial accretion timescale  $t_{acc,0}$  to the initial expansion time  $t_{exp,0}$ , defined as follows (Colpi, Shapiro, & Wasserman 1996; Zampieri et al. 1998):

$$\tilde{k} = \frac{t_{acc,0}}{t_{exp,0}} = \frac{GM_c}{c_{s0}^3} \times \frac{V_0}{R_0}, \quad (8)$$

where  $M_c$  is the mass of the compact remnant, taken to be equal to  $3M_\odot$  at the onset of the evolution<sup>2</sup>. In particular, the polytropic constant  $K$  and the initial central

temperature  $T_0$  depend on the three input parameters  $c_{s0}$ ,  $R_0$  and  $M_{env}$ , and can be written as  $K = 3c_{s0}^2/4\rho_0^{1/3}$  and  $T_0 = (3K/a_R)^{1/4} \rho_0^{1/3}$ , where  $\rho_0$  is a function of  $R_0$  and  $M_{env}$ .  $V_0$  can be expressed in terms of  $c_{s0}$ ,  $R_0$  and  $\tilde{k}$  through Eq. [8]. The dynamical interplay of the inner accreting envelope and the outer expanding ejecta can be characterized, in absence of  $^{56}\text{Ni}$  energy input, in terms of the sole parameter  $\tilde{k}$  (see Colpi et al. 1996; Zampieri et al. 1998, for details), while the initial kinetic and thermal energy of the envelope are obtained by integration.

Concerning the boundary conditions and their numerical implementation, we refer to Zampieri et al. (1998). However we recall that at the inner boundary we assume negligible pressure and radiative forces on the gas, and adopt an outgoing wave (floating) boundary for  $w_1$ . At every time step we also set the mass of the compact remnant equal to its initial mass plus the actual mass that has fallen back up to that time. At the outer boundary, we adopt free expansion for the ejecta, a non-illuminated atmosphere in radiative equilibrium for the radiation field, and synchronization of the coordinate time with the proper time of an observer comoving with the ejecta.

## 2.4. Input physics

While a complete description of the input physics adopted in the paper is reported in Balberg et al. (2000), here we summarize the most relevant aspects concerning the treatment of the Rosseland and Planck opacities, the ionization fractions, the gas equations of state, and the radioactive heating.

As for the opacity and ionization fractions, the code uses the TOPS opacities available at the LANL server (version preceding April 2000; see Magee et al. 1995), extended in the low-temperature regime ( $T < 5.8 \times 10^3$  K) using the tables of Alexander & Ferguson (1994). They are calculated with linear interpolation in temperature, density and chemical composition, considering oxygen as representative of the entire metal component in the ejecta. A more refined approach using the most up-to-date opacities and realistic post-explosive chemical composition (computed following the progenitor evolution from the main-sequence up to the explosion) will be presented in a forthcoming paper. It should be noted that these opacities are computed assuming LTE between matter and radiation, while in the SN ejecta these conditions are not strictly met near to the photosphere. Furthermore, the effect of the non-thermal excitation and ionization from gamma rays is not included in the calculation of the opacities. In order to account for it, a so-called “opacity floor” (i.e. a minimum value equal to  $0.1 \text{ cm}^2 \text{ g}^{-1}$ ) is used in all the simulations reported in this paper, following a common practice in the hydrodynamical modelling of CC-SNe (e.g. Herzig et al. 1990; Swartz, Wheeler, & Harkness 1991; Young 2004; Dessart et al. 2010).

Concerning the gas equation of state, it is approximated as an ideal gas of ions and electrons.

As far as radioactive heating is concerned, we assume that the energy released by the decays of all the radioactive isotopes present in a given mass shell is absorbed locally or escapes from the envelope. Non-local effects in-

<sup>2</sup> This value of  $M_c$  is larger than that of a typical compact remnant ensuing from CC-SN events ( $\sim 1.3\text{--}2.6M_\odot$ ; see e.g. Limongi, Straniero & Chieffi 2000), but we chose it because it helps the numerical stability of the innermost part of the flow. While the dynamical evolution of the expanding ejecta is essentially unaffected by  $M_c$ , the amount of material that falls back in the compact remnant during the evolution is slightly overestimated by a factor  $\lesssim 3\text{--}8\%$ . Clearly, detailed calculations of fallback require choosing the value of  $M_c$  more accurately.

TABLE 1  
PROPERTIES OF THE RELEVANT RADIOACTIVE ISOTOPES

Isotope	$\varepsilon_\gamma$ [erg g <sup>-1</sup> s <sup>-1</sup> ]	$\varepsilon_{e^+}$ [erg g <sup>-1</sup> s <sup>-1</sup> ]	$\tau$ [days]
<sup>56</sup> Ni	$3.90 \times 10^{10}$	0	8.8
<sup>56</sup> Co	$6.40 \times 10^9$	$2.24 \times 10^8$	111.3
<sup>57</sup> Co	$6.81 \times 10^8$	0	391.0
<sup>44</sup> Ti	$2.06 \times 10^8$	$6.54 \times 10^7$	$3.28 \times 10^4$

NOTE. — Data taken from Woosley, Pinto, & Hartmann (1989) and Shigeyama & Nomoto (1990).

duced by gamma-ray heating are not considered. This is implemented adding to the gas energy equation (Eq. [1]) a local energy source term  $Q$ , which represents the radioactive heating rate of all the relevant isotopes synthesized in the CC-SN explosion and is given by:

$$Q = \sum_i X_i \times (\varepsilon_{i,\gamma} f_i + \varepsilon_{i,e^+}) \times e^{-\frac{t}{\tau_i}}, \quad (9)$$

where  $X_i$ ,  $\tau_i$ ,  $\varepsilon_{i,\gamma}$  and  $\varepsilon_{i,e^+}$  represent the mass fraction, lifetime, energy per unit mass and unit time released by the decay of the  $i$ -th isotope in the form of  $\gamma$ -rays and positrons, respectively, and the factor  $f_i$  accounts for the fact that the  $\gamma$ -rays are not totally trapped in the envelope (for details, see Balberg et al. 2000, and references therein). The relevant radioactive nuclei considered in the present investigation and the values of their characteristic parameters are reported in Table 1. The <sup>56</sup>Co abundance is evaluated considering that the isotope <sup>56</sup>Co is involved into the nuclear decay chain <sup>56</sup>Ni  $\rightarrow$  <sup>56</sup>Co  $\rightarrow$  <sup>56</sup>Fe, so its mass as a function of the time  $t$  is determined from:

$$\begin{aligned} M_{56\text{Co}}(t) &= M_{56\text{Co},0} \times e^{-\frac{t}{\tau_{56\text{Co}}}} + \\ M_{56\text{Ni},0} \times \frac{1}{1 - \frac{\tau_{56\text{Ni}}}{\tau_{56\text{Co}}}} &\left[ e^{-\frac{t}{\tau_{56\text{Co}}}} - e^{-\frac{t}{\tau_{56\text{Ni}}}} \right] \\ &\simeq M_{56\text{Ni},0} \times \left[ e^{-\frac{t}{\tau_{56\text{Co}}}} - e^{-\frac{t}{\tau_{56\text{Ni}}}} \right], \end{aligned} \quad (10)$$

where we assume that the initial abundance of <sup>56</sup>Co is equal to zero and that  $1/(1 - \tau_{56\text{Ni}}/\tau_{56\text{Co}}) \simeq 1$ .

### 3. NUMERICAL COMPUTATIONS

#### 3.1. Preliminary tests

In order to test the dependability of the new version of the code, a few simulations have been performed with both the new and old version. The evolution starts from the same set of initial conditions reported in sect. 2.3, except for the radial distribution of <sup>56</sup>Ni that is assumed to be uniform. We varied several input parameters (number of points, location of the inner boundary, mass of the ejecta, initial radius and energy) to check the stability and accuracy of the code. In the outer expanding part of the flow (which comprises most of the mass, in practice all the envelope mass apart from the innermost  $\sim 10^{-3} M_\odot$ ) the fractional difference between the values of the variables computed with the new and old version of the code is  $\lesssim 10$ -20% (e.g., Figures 1 and 2; see also Pumo, Zampieri & Turatto 2010). The only exception is the profile of the radiative flux that differs by  $\lesssim 50\%$ . Indeed, the radiative flux depends sensitively on

the numerical treatment. The improved stability of the new version makes the profile computed by the new code more reliable. A significant difference ( $\lesssim 40\%$ ) is present also in the innermost  $\sim 10^{-3} M_\odot$  of the envelope (below  $\log R \sim 12.7$ ), where the flow starts to fall back onto the remnant. This is most likely linked to the delicate balance between the pressure gradients and the gravitational force, that determines the location of the accretion radius  $r_a$  (see Balberg et al. 2000, for details). Even a slight difference in the calculation of the gas and radiation pressures may cause a sign reversal in the velocity of the marginally bound gas shells (containing  $\lesssim 10^{-4} M_\odot$ ) located near to  $r_a$ , that start then to fall back onto the remnant instead of going outwards.

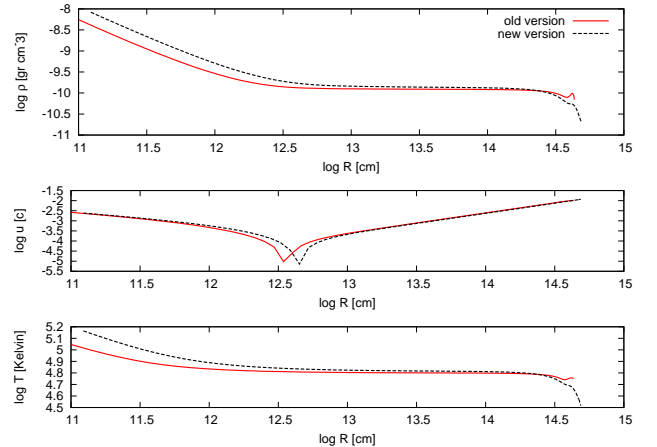


FIG. 1.— Comparison between results obtained from the old (dotted line) and new (dashed line) versions of the code. The comparison refers to a model evolved for 15 days from the breakout of the shock wave at the stellar surface, and having initial radius of  $3 \times 10^{13}$  cm, total energy of 1 foe, amount of <sup>56</sup>Ni equal to  $0.07 M_\odot$ , and the envelope mass of  $16 M_\odot$ . Top, middle, and bottom panels show the radial profiles of the gas matter density  $\rho$  (in units of g cm<sup>-3</sup>), absolute value of the fluid radial-velocity (in units of the velocity of light c) and the gas temperature (in units of Kelvin), respectively. The innermost part of the envelope, below  $\log R \sim 12.5$ -12.7, is accreting onto the central remnant and has negative velocity.

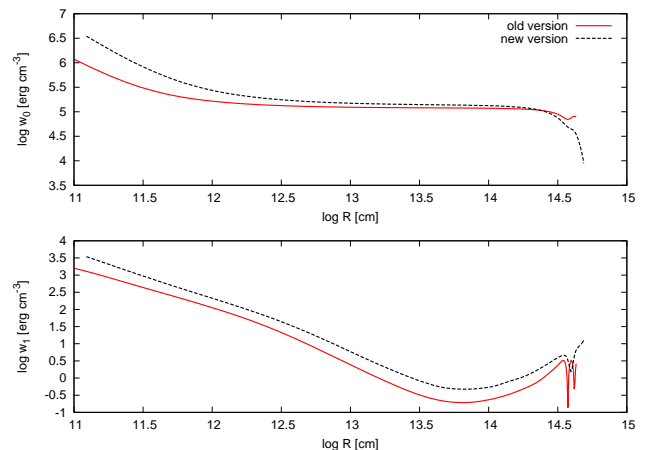


FIG. 2.— Same as Fig. 1, but for the radial profiles of the radiation energy density  $w_0$  (top panel) and the radiative flux  $w_1$  (bottom panel). Both quantities are in units of erg cm<sup>-3</sup>.

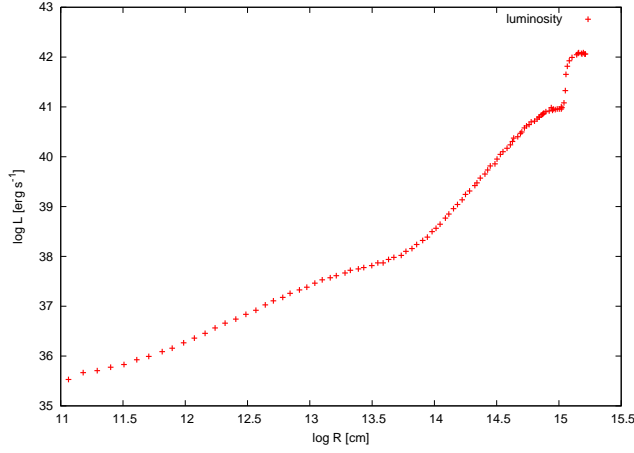


FIG. 3.— Radial profiles of the radiative luminosity at the beginning of the recombination phase for model (1) in Table 2. Less than 5% in mass of the envelope has recombined. The sharp front at  $\log R \sim 15.1$  marks the position of the recombination wave, where also the photosphere is located.

While the simulations with the old version often develop numerical instabilities, those evolved with the new version show to be stable. Several models were evolved for long times checking the long-term numerical stability of the new code during some key evolutionary stages like the radiative recombination phase. The position of the recombination front is very well traced (see Figure 3) and, consequently, it is possible to follow the post-explosion evolution of a CC-SN event in its “entirety”, from the breakout of the shock wave at the stellar surface up to the nebular stage.

### 3.2. Grid of models

Different simulations were performed with the new version of the code exploring a relatively large fraction of the parameter space related to the post-explosion evolution of a “typical” CC-SN.

In particular a total of 22 models were calculated changing the initial radius from  $3 \times 10^{12}$  to  $10^{14}$  cm, the total energy from 0.5 to 3 foe, the amount of  $^{56}\text{Ni}$  from 0.005 to  $0.070 M_{\odot}$ , and the envelope mass from 8 to  $18 M_{\odot}$  (see Table 2 for details). In the present sample, we assume that the initial thermal and kinetic energy are equal and hence three out of the four input parameters of the model ( $M_{\text{env}}$ ,  $c_{s0}$  and  $\tilde{k}$ ) are related. All the simulations were performed fixing the parameter controlling the  $^{56}\text{Ni}$  distribution at the value  $K_{\text{mix}} = 5$ . This corresponds to having  $\sim 90\%$  of the  $^{56}\text{Ni}$  in the envelope concentrated in the innermost  $\sim 3, 5, 6.5$  and  $7.5 M_{\odot}$  for the models with an envelope mass equal to 8, 12, 16 and  $18 M_{\odot}$ , respectively (see Eq. [4]).

## 4. VALIDATION OF THE NEW CODE AND PHYSICAL BEHAVIOR OF CC-SN MODELS

### 4.1. Code validation

Some of the models reported in Table 2 have been used to further validate the code against observations and by comparison with similar models reported in the literature. In particular, we have compared:

- model (1) with model (A) of Young (2004) that has a similar input parameters (i.e. total energy

TABLE 2  
MODELS PARAMETERS

Model	Radius $10^{12} [\text{cm}]$	Envelope mass $[M_{\odot}]$	Energy $[\text{foe} \equiv 10^{51} \text{ ergs}]$	$^{56}\text{Ni}$ mass $[M_{\odot}]$
1	3	16	1	0.070
2	30	18	1	0.070
3	30	8	1	0.035
4	30	12	1	0.035
5	30	12	2	0.035
6	30	16	0.5	0.070
7	30	16	1	0.005
8	30	16	1	0.010
9	30	16	1	0.020
10	30	16	1	0.035
11	30	16	1	0.045
12	30	16	1	0.055
13	30	16	1	0.070
14	30	16	1.3	0.070
15	30	16	1.6	0.070
16	30	16	1.9	0.070
17	30	16	2	0.035
18	30	16	2	0.070
19	30	16	3	0.035
20	30	16	3	0.070
21	60	16	1	0.070
22	100	16	1	0.070

of 1 foe, initial radius of  $3 \times 10^{12}$  cm,  $^{56}\text{Ni}$  mass of  $0.07 M_{\odot}$ , and  $^{56}\text{Ni}$  mixing throughout the innermost  $6 M_{\odot}$  region of the envelope);

- models (3), (4) and (10) with results of simulations performed with the semi-analytic code of Zampieri et al. (2003) and Zampieri (2007);
- model (13) with results of simulations performed with the aforementioned semi-analytic code, and with model (B) of Young (2004) that has a similar input physics (i.e. total energy of 1 foe, initial radius of  $3 \times 10^{13}$  cm,  $^{56}\text{Ni}$  mass of  $0.07 M_{\odot}$ , and  $^{56}\text{Ni}$  mixing throughout the innermost  $6 M_{\odot}$  region of the envelope);
- models (1) and (2) with observations of SN 1987A.

Figures 4 through 11 show the results of these comparisons.

The agreement between the results obtained with our code and those reported in the literature is good, considering the different initial conditions, input physics and numerical methods adopted (see Figures 4 through 9). In particular, we found overall consistency with the results of the semi-analytic code of Zampieri et al. (2003) and Zampieri (2007), that serves also as cross validation of the latter.

However, in some simulations there are somewhat significant discrepancies in the photospheric velocity and temperature during the early evolution ( $\lesssim 10$ -20 days). The fractional difference between the values of the variables computed with our new code and those computed with other codes is  $\gtrsim 15$ -30%. In particular, the disagreement with the models computed by Young (2004) is probably due to the initial density profile. Indeed, in this investigation we limited our analysis to simplified initial conditions, assuming that gas behaves as a polytrope and that  $\rho \propto T^3 \propto [\sin(\pi x)/(\pi x)]^{3/4}$  (see Eq. [6]). However, the external layers of a SN typically have a steeper

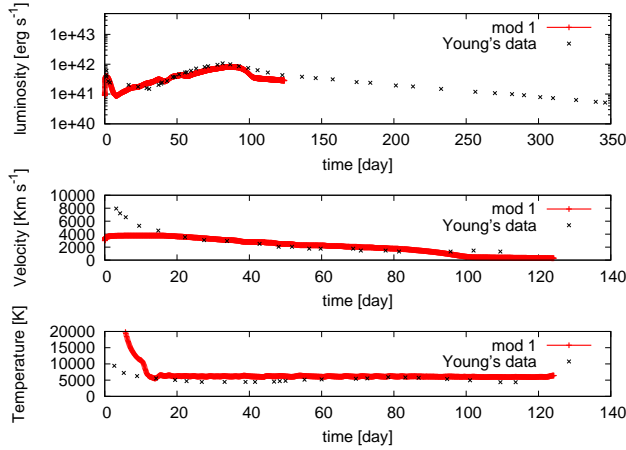


FIG. 4.— Evolution of the main observables for model (1) in Table 2 and model (A) of Young (2004) (see text for details). Top, middle, and bottom panels show the bolometric light curve, photospheric velocity and temperature as a function of time, respectively.

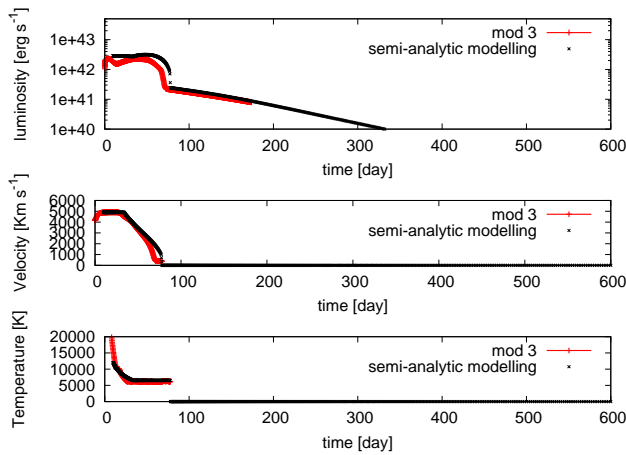


FIG. 5.— Same as Fig. 4, but for the comparison between model (3) and the corresponding model computed with the semi-analytic code (see text for details).

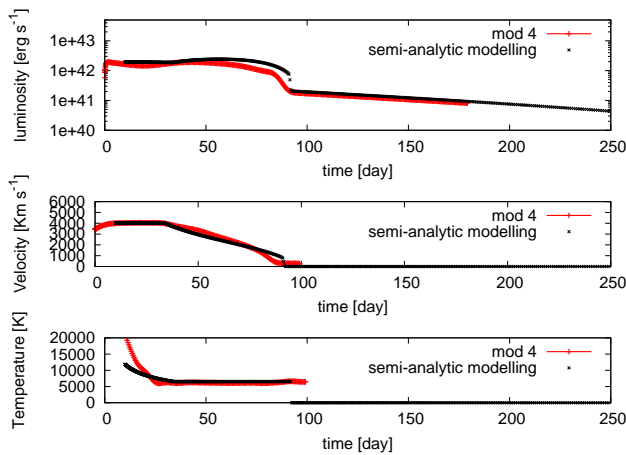


FIG. 6.— Same as Fig. 4, but for the comparison between model (4) and the corresponding model computed with the semi-analytic code (see text for details).

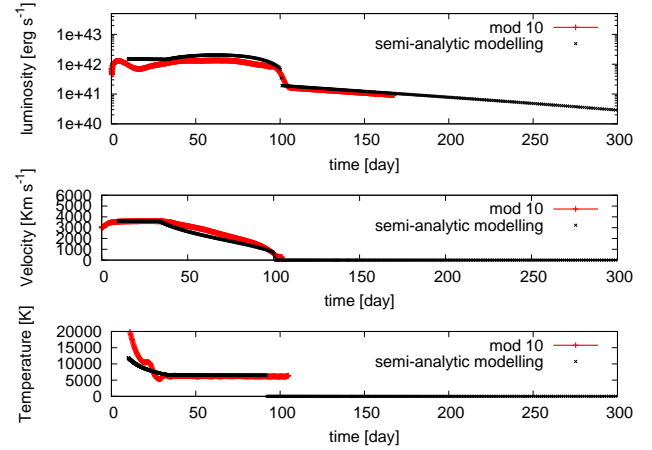


FIG. 7.— Same as Fig. 4, but for the comparison between model (10) and the corresponding model computed with the semi-analytic code (see text for details).

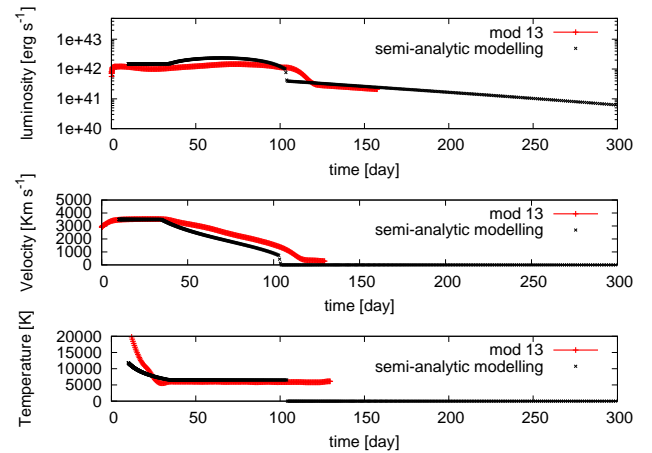


FIG. 8.— Same as Fig. 4, but for the comparison between model (13) and the corresponding model computed with the semi-analytic code (see text for details).

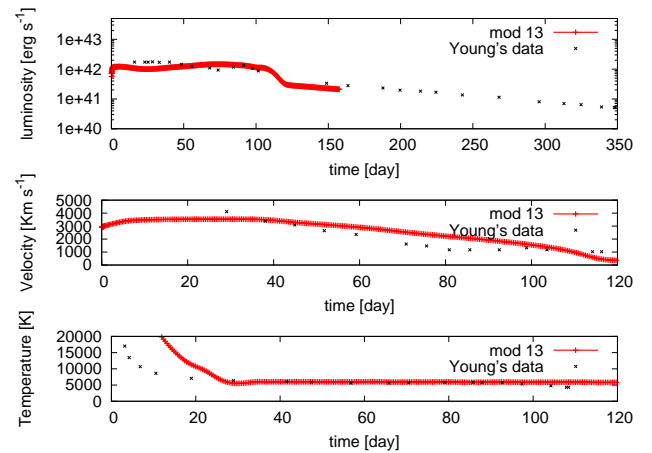


FIG. 9.— Same as Fig. 4, but for the comparison between our model (13) and model (B) of Young (2004) (see text for details).

power-law distribution caused by the acceleration of the

shock wave through the exponentially decaying density profile of the progenitor star. These layers ( $0.01\text{--}0.1 M_{\odot}$ )



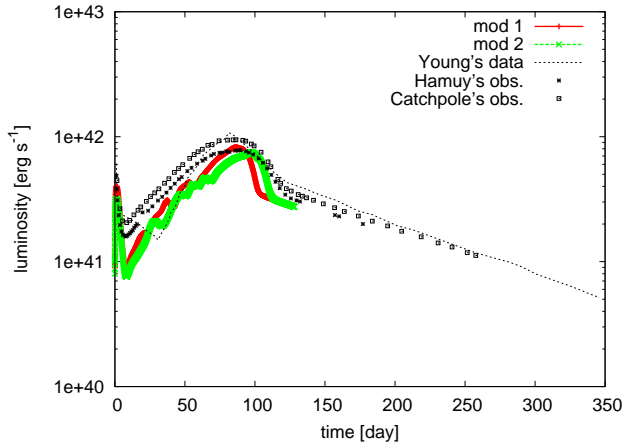


FIG. 10.— Bolometric light curves of models (1) and (2) compared to the light curve of SN 1987A (taken from Catchpole et al. 1987, 1988 and Hamuy et al. 1988). The best fitting model of Young (2004) is also reported for comparison.

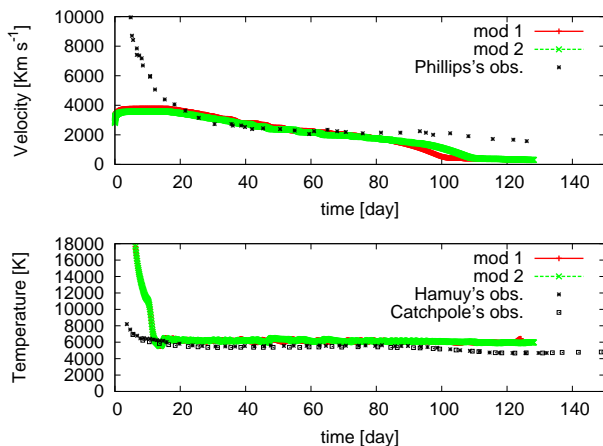


FIG. 11.— Evolution of the photospheric velocity (top panel) and temperature (bottom panel) for models (1) and (2) compared to the corresponding quantities of SN 1987A (taken from Catchpole et al. 1987, 1988, Hamuy et al. 1988 and Phillips et al. 1988).

in mass) are set into high-velocity and are not homologously expanding (see also Utrobin 2004; Woosley 1988). During the first  $\sim 10$ -20 days after the explosion, the photosphere is located in this shell, which is then cooler and has a higher velocity than the bulk of the ejecta. This results in a different evolution of the photospheric temperature and velocity. A better agreement during this phase is found with the semi-analytic code, that adopts a uniform density distribution. Some disagreement is present also at late-times ( $\gtrsim 80$ -110 days), that is probably related to differences in the treatment of ionization balance and in the adopted opacities (including the opacity floor).

Despite the limitations of our simplified initial conditions, also the comparison with the bolometric light curve of SN 1987A is satisfactory. We are able to reproduce its main features (peak luminosity and phase at maximum) with models having initial radius of  $3 \times 10^{12}$  cm, total initial energy of 1 foe, amount of  $^{56}\text{Ni}$  equal to  $0.07 M_{\odot}$ , and envelope mass ranging between 16 and  $18 M_{\odot}$  (models (1) and (2) in Figures 10 and 11). The agreement can

be considered satisfactory also because we did not perform any “fine-tuning” of the initial composition which is typically needed in order to accurately reproduce the observed shape (width and rise to peak) of the bolometric light curve of SN 1987A (e.g. Woosley 1988; Utrobin 2004). Further residual differences may also be caused by the absence of non-thermal ionization from gamma rays in our models. The time evolution of the photospheric velocity and temperature of SN 1987A is also well reproduced by models (1) and (2), apart from the differences in the early and the late-time evolution due to the same reasons mentioned above. Moreover, as can be seen from Figure 10, the luminosity in the radioactive tail predicted by the model is lower than the observed one. This is a consequence of fallback occurring during the evolution. We found that the innermost  $\sim 0.01 M_{\odot}$  of the envelope, containing  $\sim 2.4 \times 10^{-3} M_{\odot}$  of  $^{56}\text{Ni}$ , have been accreted onto the central remnant.

#### 4.2. Reference case

To give a general overview of the post-explosion evolution of a “typical” CC-SN, we focus on the properties of our model (13) that has rather common initial parameters. The evolution is determined by the thermodynamics of the expanding ejecta. The internal energy deposited by the shock wave and that released by gamma-ray radioactive decays are used to expand the ejecta and power light curve. The evolution is characterized by three phases in which different heating and emission mechanisms dominate. During the first phase (diffusive phase), the envelope is completely ionized and optically thick, and the emission is due to the release of internal energy on a diffusion timescale. In the second phase (recombination phase), the ejecta are recombining and the emission is dominated by the sudden release of energy caused by the receding motion of the wavefront through the envelope. During the last phase (radioactive-decay phase or radioactive tail), the envelope is recombined and optically thin to optical photons, and the emission comes from the thermalization of the energy deposited by gamma-ray photons. Observationally, the first two phases coincide with what is usually defined the plateau or photospheric phase, while the last phase is referred to as nebular phase.

Figures 12 through 14 show the physical properties of model (13) at three different times, taken to be representative of the aforementioned three phases. Moreover Figures 15 through 18 show the evolution of the photospheric radius, and the radial profiles of the photospheric velocity and temperature in more detail.

During the first phase ( $\lesssim 35$  days), the radiation diffusion time-scale is much longer than the expansion time-scale, and the cooling induced by photon diffusion is negligible. Although the internal energy decreases because of expansion, the temperature and the density are sufficiently high that the envelope remains completely ionized and optically thick (Figures 12, 15 and 16). The photospheric radius, which is located in the outermost shell, increases by a factor  $\sim 40$  in  $\sim 35$  days from the breakout of the shock wave at the stellar surface (see Figure 18). The expansion is nearly homologous, as witnessed by the nearly constant value of the photospheric velocity.

At  $\sim 35$  days, in the outermost layers the temperature reaches  $\sim 6000$  K and hydrogen starts to recombine. This



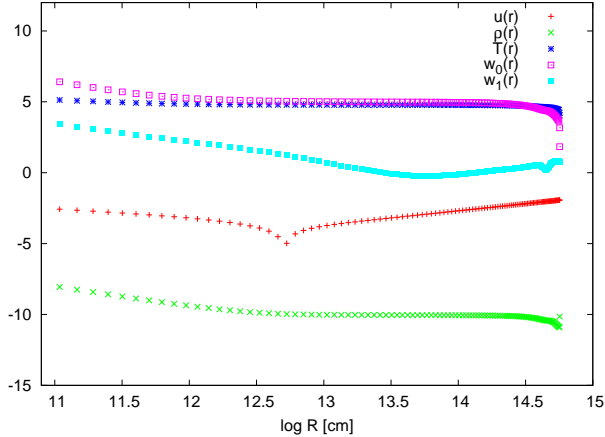


FIG. 12.— From bottom to top, radial profiles of the gas matter density (in units of  $\text{g cm}^{-3}$ ), absolute value of the fluid radial-velocity (in units of  $\text{c}$ ), radiative flux (in units of  $\text{erg cm}^{-3}$ ), gas temperature (in units of Kelvin), and radiation energy density (in units of  $\text{erg cm}^{-3}$ ) as a function of radius (in units of  $\text{cm}$ ). All scales on the  $y$  axis are logarithmic. The radial profiles refer to model (13) at 18 days from the breakout of the shock wave at the stellar surface. The innermost part of the envelope, below  $\log R \sim 12.7$ , is accreting onto the central remnant and the radial-velocity there is negative.

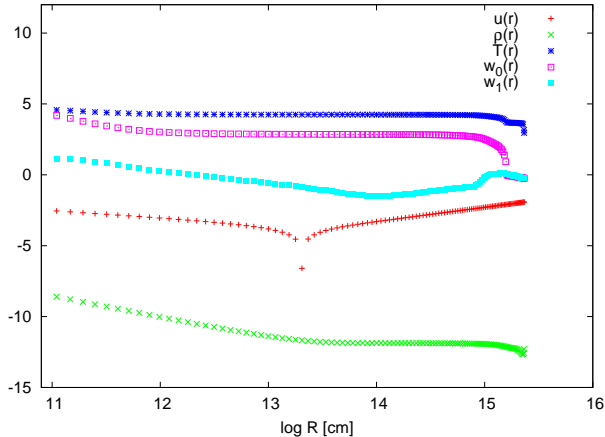


FIG. 13.— Same as Fig. 12, but for 75 days from the breakout of the shock wave at the stellar surface. The boundary of the innermost accreting part of the envelope is at  $\log R \sim 13.3$ .

marks the beginning of the recombination phase. During this phase, the evolution is characterized by the fast recombination of the outer zone, leading to the formation of a recombination wave (RW) that moves inward (in mass) like a flame. In the external layers, the temperature drops below  $\sim 6000$  K and, consequently, the internal energy is efficiently radiated away because of the sudden decrease of the opacity (see Figures 13, 15 and 16). The RW marks the boundary between the inner envelope that is optically thick, ionized and hot ( $> 6000$  K), and the outer layers that are optically thin, recombined and cooler ( $\lesssim 6000$  K). The photosphere moves inward (in mass) following the motion of the RW and allows photons to escape sooner than they would if the photosphere were fixed in the outmost layer of the envelope. As a consequence, advective cooling induced by the RW motion becomes dominant. The energy radiated away at this

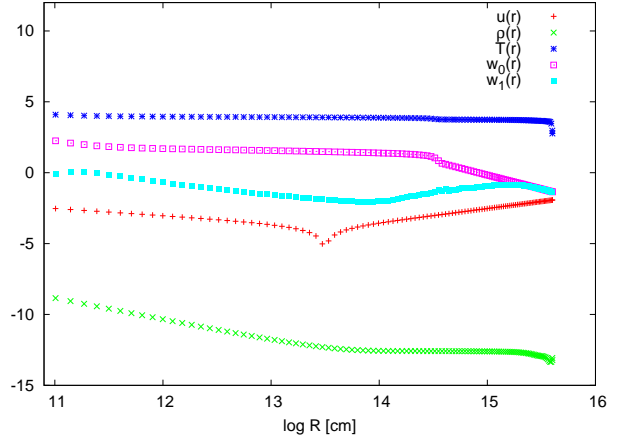


FIG. 14.— Same as Fig. 12, but for 130 days from the breakout of the shock wave at the stellar surface. The boundary of the innermost accreting part of the envelope is at  $\log R \sim 13.4$ .

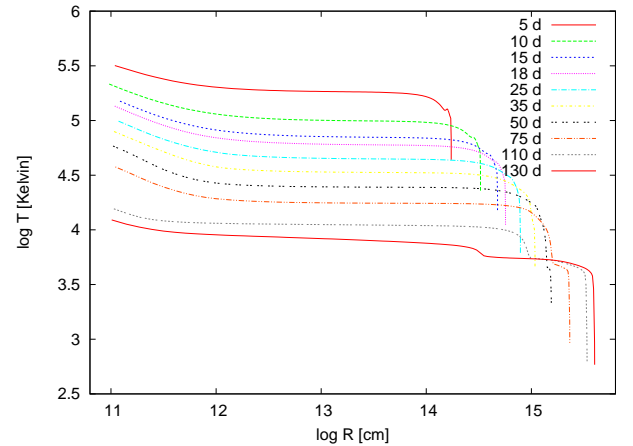


FIG. 15.— Gas temperature as a function of radius for model (13) at different times. Labels indicate the time (in units of days) from the breakout of the shock wave at the stellar surface.

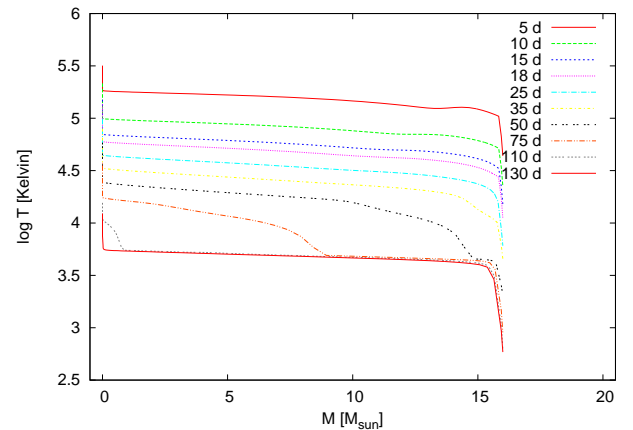


FIG. 16.— Same as Fig. 15, but for the gas temperature as a function of mass.

stage is the sum of the residual internal energy left over after expansion and that liberated during recombination. The energy deposited by gamma-rays becomes signifi-

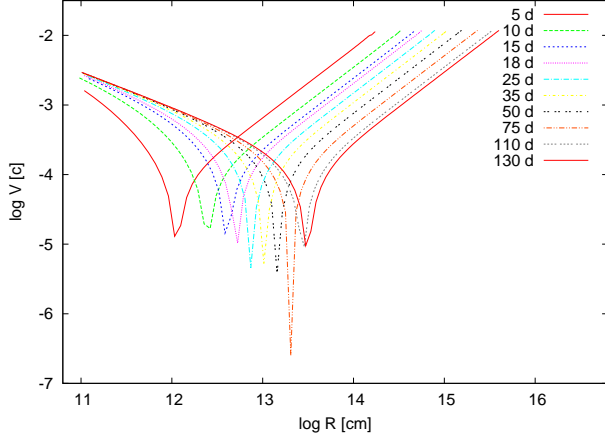


FIG. 17.— Absolute value of the fluid radial-velocity as a function of radius for model (13) at different times. Labels indicate the time (in unit of days) from shock breakout. The minimum of each curve marks the boundary of the inner accreting zone (where the radial-velocity is negative).

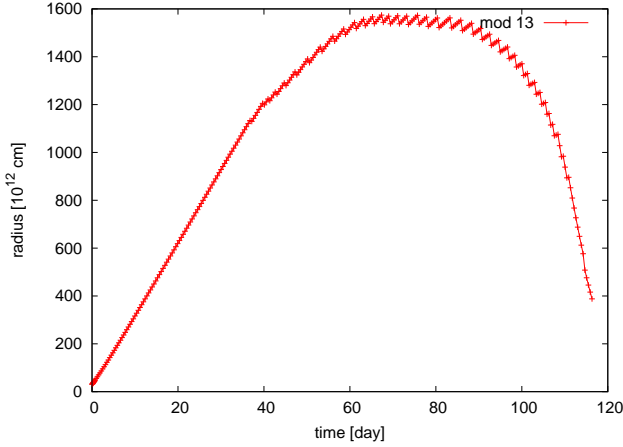


FIG. 18.— Evolution of the photospheric radius for model (13).

cant only when the RW reaches the innermost zones, full of  $^{56}\text{Ni}$  (see also Young 2004; Bersten et al. 2011). The bolometric luminosity, initially almost constant, plummets when the RW reaches the center (see the top panel in Figure 9). The bulk of the envelope ( $\sim 95\%$  in mass) is recombined after  $\sim 110$  days from the breakout of the shock wave at the stellar surface (see Figure 16). The photospheric velocity decreases because the photosphere moves inward with the RW, reaching inner and slower layers as time elapses (see the middle panel in Figure 9).

The velocity of propagation of the RW is determined by the physical conditions in the envelope, in particular the temperature, density, amount of  $^{56}\text{Ni}$  and their distributions. The motion of the photospheric radius for a distant observer is the result of the interplay between the inward motion of the RW in mass and the expansion of the ejecta. Consequently, as shown in Figure 18, from  $\sim 35$  up to  $\sim 65$  days, the photospheric radius increases, while later on it stays at an almost constant (eulerian) radial coordinate for about  $\sim 20$  days. Then, the photosphere starts to recede in radius and the luminosity plummets.

The duration and steepness of the transition from the plateau to the radioactive tail depend on the  $^{56}\text{Ni}$  mass (see sect. 4.3) and its distribution in the ejecta. During this last phase, the evolution is completely governed by the deposition and reprocessing of the energy released from the radioactive decay of  $^{56}\text{Co}$  into  $^{56}\text{Fe}$ . The envelope is sufficiently opaque to the gamma-rays emitted in the radioactive decays that a large fraction of them are effectively absorbed and their energy deposited in the ejecta. This energy is easily radiated away by lower energy photons on a timescale much shorter than the expansion timescale. Also the heating time, which is essentially the  $^{56}\text{Co}$  decay time, is smaller than the expansion time and, hence, the loss of internal energy due to expansion is negligible. Therefore, the bolometric luminosity is the total heating rate from the radioactive decays, proportional to the mass of  $^{56}\text{Ni}$  synthesized in the explosion (see also sect. 4.3).

#### 4.3. Effects of varying the initial parameters on the light curve, photospheric velocity and temperature

The sample of models (reported in Table 2) enabled us to study the effects of the variation of each parameter (namely, envelope mass  $M_{\text{env}}$ , initial outer radius  $R_0$ , total ejecta energy  $E$ , and amount of  $^{56}\text{Ni}$   $M_{\text{Ni}}$ ) on the main observables, while holding the others fixed. Figures 19 through 22 summarize the results of this analysis. We note, however, that this investigation is not meant to be a realistic model survey for a detailed quantitative comparison with observations, because it does not include models computed starting from realistic initial conditions. This is postponed to a follow-up investigation.

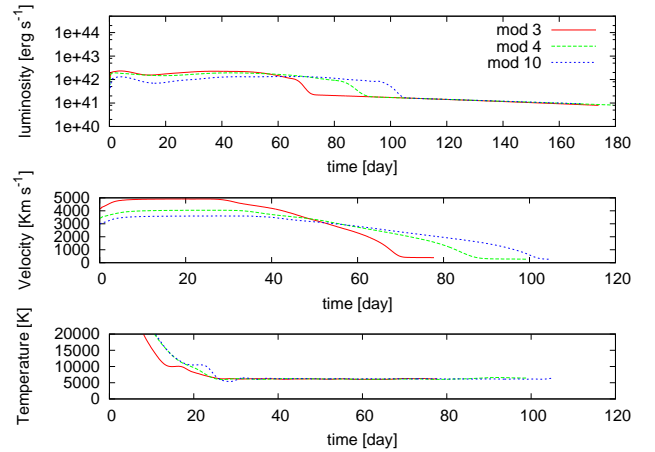


FIG. 19.— Effects of varying the envelope mass on the main observables for models (3), (4), and (10) with  $M_{\text{env}} = 8, 12$ , and  $16M_{\odot}$ , respectively. The models (see Table 2) have the same initial radius ( $R_0 = 3 \times 10^{13}$  cm), total energy ( $E = 1$  foe), and amount of  $^{56}\text{Ni}$  ( $M_{\text{Ni}} = 0.035M_{\odot}$ ). Top, middle, and bottom panels show the bolometric light curve, photospheric velocity and temperature as a function of time, respectively.

As can be seen from Figure 19, more massive envelopes lead to a fainter bolometric light curve during the diffusive phase, a longer plateau phase, a hotter photospheric temperature during the first  $\sim 20$ -30 days, a lower photospheric velocity up to  $\sim 50$  days and a slower decline at

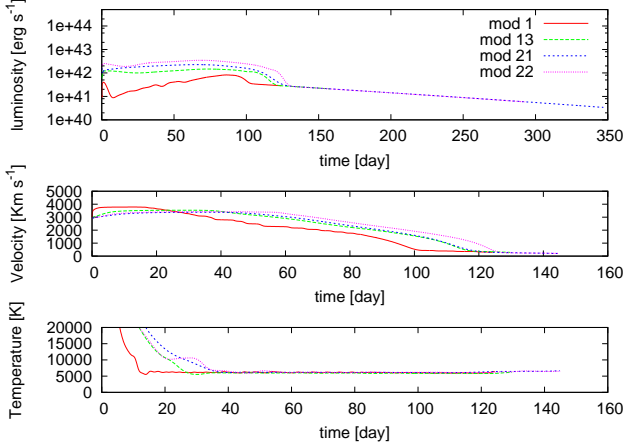


FIG. 20.— Same as Fig. 19, but for the initial radius. The lines refer to models (1), (13), (21), and (22) with  $R_0 = 3 \times 10^{12}$ ,  $3 \times 10^{13}$ ,  $6 \times 10^{13}$ , and  $10^{14}$  cm, respectively. The models (see Table 2) have the same envelope mass ( $M_{env} = 16M_\odot$ ), total energy ( $E = 1$  foe), and amount of  $^{56}\text{Ni}$  ( $M_{Ni} = 0.07M_\odot$ ).

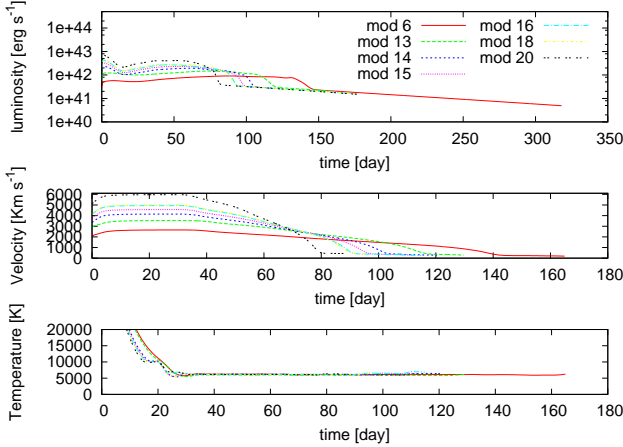


FIG. 21.— As for Fig. 19, but for the total energy. The lines refer to models (6), (13), (14), (15), (16), (18), and (20) with  $E = 0.5$ , 1, 1.3, 1.6, 1.9, 2, and 3 foe, respectively. The models (see Table 2) have the same initial radius ( $R_0 = 3 \times 10^{13}$  cm), envelope mass ( $M_{env} = 16M_\odot$ ), and amount of  $^{56}\text{Ni}$  ( $M_{Ni} = 0.07M_\odot$ ).

longer times. As known, this behavior is a consequence of the increase in the diffusion timescale with increasing envelope mass, that causes a slower leakage of photons and hence a lower luminosity, longer plateau and higher temperature. At the same time, increasing the mass and keeping the initial kinetic energy constant (which is half of the total energy; see Sect. 3.2) results in a smaller photospheric velocity during the first weeks and a slower decline later on, caused by the slower motion of the RW in a higher density envelope.

The effects of varying the initial radius are shown in Figure 20. Larger values of  $R_0$  cause a higher luminosity during the diffusive and recombination phases, a longer plateau, and a smaller photospheric velocity up to  $\sim 25$  days. The higher luminosity  $L$  during the diffusive phase is caused by the fact that  $L$  is proportional to the initial radius  $R_0$  (e.g. Arnett 1996), as the radiative flux  $F \propto T^4/(\kappa_{es}\rho_0 R_0) \propto R_0^{-1}$ . The lower initial photospheric velocity, longer plateau and higher initial temper-

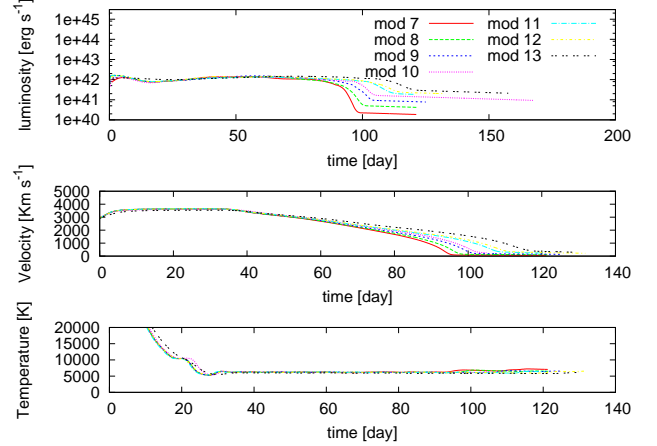


FIG. 22.— As for Fig. 19, but for the  $^{56}\text{Ni}$  mass. The lines refer to models (7), (8), (9), (10), (11), (12), and (13) with  $M_{Ni} = 0.005$ , 0.01, 0.02, 0.035, 0.045, 0.055, and  $0.070M_\odot$ , respectively. The models (see Table 2) have the same initial radius ( $R_0 = 3 \times 10^{13}$  cm), envelope mass ( $M_{env} = 16M_\odot$ ), and total energy ( $E = 1$  foe).

ature are a consequence of the smaller  $PdV$  work done by bigger expanding envelopes. Less internal energy is initially converted into kinetic energy, the expansion is slower and more energy remains available for heating up the envelope.

Figure 21 shows the effects of varying the total energy (with ratio between thermal and kinetic energy equal to 1; see Sect. 3.2). Increasing it causes a higher luminosity in the bolometric light curve during the diffusive and recombination phases, a shorter plateau, a higher photospheric velocity up to  $\sim 60 - 70$  days and a faster decline at longer times. The early behavior can be easily understood as a consequence of the larger internal energy dumped in the ejecta, that increases their initial velocity and accelerates all the evolutionary stages.

As for the effects of varying  $^{56}\text{Ni}$  (see Figure 22), increasing it makes the plateau phase longer and causes a slower decline of the bolometric light curve towards the radioactive tail. Furthermore, as  $M_{Ni}$  increases, also the decline of the photospheric velocity is slower, while the bolometric luminosity becomes higher during the radioactive tail. All these effects are related to the increased heating provided by the larger amount of  $^{56}\text{Ni}$  concentrated in the innermost part of the envelope, that increases the internal energy and luminosity especially at late phases and slows down the motion of the RW (e.g. Arnett 1996; Hamuy 2003b; Nadyozhin 2003).

## 5. SUMMARY AND FINAL COMMENTS

We developed a general-relativistic, radiation hydrodynamics, Lagrangian code tailored to the radiation-hydrodynamical modelling of CC-SNe, whose distinctive features are an accurate treatment of radiative transfer coupled to relativistic hydrodynamics, a self-consistent treatment of the evolution of the innermost ejecta taking into account the gravitational effects of the central compact remnant, and a fully implicit Lagrangian approach to the solution of the coupled non-linear finite difference system of equations. The latter property represents the major novelty of this code, that is based on a previous version originally developed for studying fall

back in the aftermath of a SN explosion (Zampieri et al. 1998; Balberg et al. 2000).

With this code, a total of 22 models of hydrogen-rich CC-SNe were calculated, enabling us to (a) validate the code against observations and similar models reported in the literature, and (b) study the role of the “main” parameters affecting the post-explosion evolution of the CC-SN events (namely the ejected mass, the progenitor radius, the explosion energy, and the amount of  $^{56}\text{Ni}$ ).

The aforementioned grid of models permitted us also to explore possible correlations among different quantities that can be measured from the light curve and spectra, and investigate how variations of basic parameters combine together to produce them. This is particularly relevant in connection with the possibility to calibrate hydrogen-rich CC-SNe to turn them into usable distance indicators. Indeed, in recent years growing attention has been devoted to the construction of Hubble diagrams using hydrogen-rich CC-SN events (e.g. Nugent et al. 2006; Olivares et al. 2010) in order to derive cosmological parameters independently of the usual method based on type Ia SNe (e.g. Riess et al. 1998; Perlmutter et al. 1999; Astier et al. 2006; Wood-Vasey et al. 2007; Hicken et al. 2009; Freedman et al. 2009).

Although a complete study using a more extended grid of models calculated from realistic initial conditions is presently under investigation, here we mention some preliminary results obtained for the sample of 22 models presented in this paper. Indeed, despite the limitations related to the use of simplified initial conditions, we are able to reproduce the power-law relation between the luminosity and the photospheric velocity (both measured at day 50 from the breakout of the shock wave at the stellar surface) found in the observational sample of Hamuy & Pinto (2002). The index of the theoretical correlation is equal to  $3.13 \pm 0.29$ , in good agreement within the errors with the value  $3.03 \pm 0.37$  reported by Hamuy & Pinto (2002). Our models confirm also the anti-correlation between the light curve slope at the so-called inflection time  $t_i$  (when the semi-

logarithmic derivative of the luminosity  $L$  at the end of the plateau is maximum) and the amounts of  $^{56}\text{Ni}$  inferred by Elmhamdi, Chugai, & Danziger (2003) on observational bases. Finally, we found a very promising calibration relation between the luminosity  $L_*$  at a generic time  $t_*$  during the plateau and the characteristic time  $t_c = t_{0.4} - t_*$ , where  $t_{0.4}$  is the time when  $L_*$  decreases by a factor 2.5. These last two relations may represent useful tools for calibrating hydrogen-rich CC-SNe using only photometric data. In particular, for type II plateau SNe the latter relation is essentially independent of the explosion epoch as  $L_*$  is approximately constant during the plateau.

We are working at present to check the validity of these preliminary results against a more extended grid of models that is being computed from realistic initial conditions. We plan to check these calibrations also against observations using well sampled light curves of hydrogen-rich CC-SNe that are being collected within the dedicated large program “Supernova Variety and Nucleosynthesis Yields” (P.I. S. Benetti) presently running at the European Southern Observatory and the Telescopio Nazionale Galileo. The aforementioned grid of models will also serve to build an extended database to be compared with observations of single SNe in order to infer their physical properties, in analogy to what already being done using models with simplified initial conditions (e.g. SN 2007od; see Inserra et al. 2011).

Our medium- and long-term goal is the development of a sort of “CC-SNe Laboratory” in which our code is interfaced, in input, with other codes dealing with the calculations of the pre-SN evolution (see e.g. Limongi & Chieffi 2003, and references therein) and explosive nucleosynthesis (see e.g. Chieffi & Limongi 2004, and references therein), and in output with a spectral synthesis code (see e.g. Mazzali 2000; Mazzali & Lucy 1993). This will allow us to describe the evolution of a CC-SN event in a “self-consistent” way from the evolutionary stages preceding the main sequence up to the post-explosive phases as a function of initial mass, metallicity, stellar rotation, and mass loss history of the CC-SN progenitor.

## APPENDIX

### FINITE DIFFERENCE EQUATIONS

We start from Eqs. [1], [2] and [3], write  $r_{,t} = au$ , and express  $b_{,t}/b = -(\rho r^2)_{,t}/\rho r^2$  in terms of the continuity equation (Eqs. [8] and [4] in Zampieri et al. 1998). We then discretize the spatial computational domain (in Lagrangian mass  $\mu$ ) dividing it into a grid of  $j_{max}$  zones (equal to 110 in our simulations), where a constant fractional increment in grid spacing between successive zones  $\alpha$  is used. This fractional increment is calculated from the following relation:

$$\mu_{max} = \mu_{min} + \sum_{j=j_{min}}^{j_{max}-1} \Delta\mu_{j+1/2}, \quad (\text{A1})$$

where  $\mu_{min} = \mu_{j_{min}}$  is the inner boundary of the grid in Lagrangian mass,  $\mu_{max} = \mu_{j_{max}}$  is the outer boundary (fixed during a simulation due to the conservation of the envelope mass), and  $\Delta\mu_{j+1/2} \equiv \mu_{j+1} - \mu_j = \alpha\Delta\mu_{j-1/2}$ . At the beginning of the simulation,  $\mu_{min} = 0$ ,  $\mu_{max} = M_{env}$ , and the mass contained within the first shell  $\Delta\mu_{1/2}$  is fixed by the requirement that the radial spacing between the first two shells is 30% of the inner radial boundary  $r_{in} = r(\mu_{min})$ . During the evolution, if the inner edge of the innermost zone crosses  $r_{in}$ , it is removed from the calculation and a regridding of all the variables is performed so as to have  $j_{max}$  zones at all times. In particular, the new inner boundary is set equal to  $\mu_{j_{min}+l}$ , where  $l$  is the number of zones that have crossed  $r_{in}$ , and the new fractional increment  $\alpha$  is calculated from Eq. [A1] with the new value of inner boundary. Afterwards, all the variables are interpolated on the new grid.

As for the spatial centering of the variables,  $B = a_R T^4$  and  $w_0$  are evaluated at mid zone ( $\mu_{j-1/2}$ ), while  $w_1$  at

zone boundary ( $\mu_j$ ). Concerning the time centering, all quantities are evaluated at the full time level  $t^n$ . With this centering and following a standard Lagrangian approach for the discretization of the equations and the derivatives, the finite difference form of Eqs. [1], [2] and [3] can be written as:

$$\begin{aligned} \frac{\epsilon_{j-1/2}^{n+1} - \epsilon_{j-1/2}^n}{\Delta t^{n+1/2}} + a_{j-1/2}^{n+1/2} (k_P)_{j-1/2}^{n+1/2} \left[ B_{j-1/2}^{n+1/2} - (w_0)_{j-1/2}^{n+1/2} \right] + \\ + \frac{p_{j-1/2}^{n+1/2}}{\Delta t^{n+1/2}} \left( \frac{1}{\rho_{j-1/2}^{n+1}} - \frac{1}{\rho_{j-1/2}^n} \right) = 0 \end{aligned} \quad (\text{A2})$$

$$\begin{aligned} \frac{(w_0)_{j-1/2}^{n+1} - (w_0)_{j-1/2}^n}{\Delta t^{n+1/2}} - a_{j-1/2}^{n+1/2} (k_P)_{j-1/2}^{n+1/2} \rho_{j-1/2}^{n+1/2} \left[ B_{j-1/2}^{n+1/2} - (w_0)_{j-1/2}^{n+1/2} \right] + \\ + (w_0)_{j-1/2}^{n+1/2} a_{j-1/2}^{n+1/2} \left[ \left( \frac{4}{3} + f_{j-1/2}^{n+1/2} \right) \frac{1}{(r^2)_{j-1/2}^{n+1/2}} \times \right. \\ \times \left. \frac{u_j^{n+1/2} (r_j^{n+1/2})^2 - u_{j-1}^{n+1/2} (r_{j-1}^{n+1/2})^2}{r_j^{n+1/2} - r_{j-1}^{n+1/2}} - 3 \left( f \frac{u}{r} \right)_{j-1/2}^{n+1/2} \right] + \\ + \left( \frac{\Gamma}{ar^2} \right)_{j-1/2}^{n+1/2} \left[ \frac{(w_1)_j (a_j)^2 (r_j)^2 - (w_1)_{j-1} (a_{j-1})^2 (r_{j-1})^2}{r_j - r_{j-1}} \right]^{n+1/2} + \\ - \left[ \frac{4\pi r a}{\Gamma} \left( \frac{4}{3} + f \right) w_0 w_1 \right]_{j-1/2}^{n+1/2} = 0 \end{aligned} \quad (\text{A3})$$

$$\frac{(w_1)_j^{n+1} - (w_1)_j^n}{\Delta t^{n+1/2}} + \frac{(F_w)^{n+1/2} (w_1)_j^{n+1/2}}{\Delta t^{n+1/2}} - \frac{(H_w)^{n+1/2}}{\Delta t^{n+1/2}} = 0, \quad (\text{A4})$$

where

$$B_{j-1/2}^{n+1/2} = \frac{B_{j-1/2}^n + B_{j-1/2}^{n+1}}{2} \quad (\text{A5})$$

$$(w_0)_{j-1/2}^{n+1/2} = \frac{(w_0)_{j-1/2}^n + (w_0)_{j-1/2}^{n+1}}{2} \quad (\text{A6})$$

$$F_w = \Delta t^{n+1/2} a_j^{n+1/2} \left[ (k_R)_j \rho_j + \frac{2}{r_j} \frac{u_{j+1/2} r_{j+1/2} - u_{j-1/2} r_{j-1/2}}{r_{j+1/2} - r_{j-1/2}} \right]^{n+1/2} \quad (\text{A7})$$

$$\begin{aligned} H_w = \Delta t^{n+1/2} \left\{ \frac{8\pi a_j r_j}{\Gamma_j} (w_1)_j^2 - a_j \Gamma_j \left[ \frac{(1/3 + f_{j+1/2}) (w_0)_{j+1/2} - (1/3 + f_{j-1/2}) (w_0)_{j-1/2}}{r_{j+1/2} - r_{j-1/2}} \right] + \right. \\ \left. - \Gamma_j \left( \frac{4}{3} + f_j \right) (w_0)_j \frac{a_{j+1/2} - a_{j-1/2}}{r_{j+1/2} - r_{j-1/2}} + 3 \frac{a_j \Gamma_j}{r_j} f_j (w_0)_j \right\}^{n+1/2}. \end{aligned} \quad (\text{A8})$$

As  $\epsilon$ ,  $p$ ,  $k_R$  and  $k_P$  are in general rather complex, non-linear functions of  $\rho$  and  $B$  (see, e.g., Eqs. [14] and [15] in Zampieri et al. 1998), relations [A2]-[A4] form a highly non-linear system of  $(3j_{max}-3)$  equations having  $(3j_{max}-3)$  unknowns, that we solve by means of the Newton-Raphson iterative method (see, e.g., Press et al. 1996, for details). Using this approach, the finite difference equations are linearized and solved iteratively for the corrections at the new

time level  $t^{n+1}$  starting from an initial guess. The equations for the corrections are:

$$\left\{ \begin{array}{l}
 \sum_{j_{min}+1}^{j_{max}} \left( \frac{\partial F_{A2}(j_{min}+1)}{\partial B_{j-1/2}} \Delta B_{j-1/2} + \frac{\partial F_{A2}(j_{min}+1)}{\partial (w_0)_{j-1/2}} \Delta (w_0)_{j-1/2} + \frac{\partial F_{A2}(j_{min}+1)}{\partial (w_1)_j} \Delta (w_1)_j \right) = -F_{A2}(j_{min}+1) \\
 \sum_{j_{min}+1}^{j_{max}} \left( \frac{\partial F_{A3}(j_{min}+1)}{\partial B_{j-1/2}} \Delta B_{j-1/2} + \frac{\partial F_{A3}(j_{min}+1)}{\partial (w_0)_{j-1/2}} \Delta (w_0)_{j-1/2} + \frac{\partial F_{A3}(j_{min}+1)}{\partial (w_1)_j} \Delta (w_1)_j \right) = -F_{A3}(j_{min}+1) \\
 \sum_{j_{min}+1}^{j_{max}} \left( \frac{\partial F_{A4}(j_{min}+1)}{\partial B_{j-1/2}} \Delta B_{j-1/2} + \frac{\partial F_{A4}(j_{min}+1)}{\partial (w_0)_{j-1/2}} \Delta (w_0)_{j-1/2} + \frac{\partial F_{A4}(j_{min}+1)}{\partial (w_1)_j} \Delta (w_1)_j \right) = -F_{A4}(j_{min}+1) \\
 \dots\dots\dots = \dots\dots\dots \\
 \sum_{j_{min}+1}^{j_{max}} \left( \frac{\partial F_{A2}(j)}{\partial B_{j-1/2}} \Delta B_{j-1/2} + \frac{\partial F_{A2}(j)}{\partial (w_0)_{j-1/2}} \Delta (w_0)_{j-1/2} + \frac{\partial F_{A2}(j)}{\partial (w_1)_j} \Delta (w_1)_j \right) = -F_{A2}(j) \\
 \sum_{j_{min}+1}^{j_{max}} \left( \frac{\partial F_{A3}(j)}{\partial B_{j-1/2}} \Delta B_{j-1/2} + \frac{\partial F_{A3}(j)}{\partial (w_0)_{j-1/2}} \Delta (w_0)_{j-1/2} + \frac{\partial F_{A3}(j)}{\partial (w_1)_j} \Delta (w_1)_j \right) = -F_{A3}(j) \\
 \sum_{j_{min}+1}^{j_{max}} \left( \frac{\partial F_{A4}(j)}{\partial B_{j-1/2}} \Delta B_{j-1/2} + \frac{\partial F_{A4}(j)}{\partial (w_0)_{j-1/2}} \Delta (w_0)_{j-1/2} + \frac{\partial F_{A4}(j)}{\partial (w_1)_j} \Delta (w_1)_j \right) = -F_{A4}(j) \\
 \dots\dots\dots = \dots\dots\dots \\
 \sum_{j_{min}+1}^{j_{max}} \left( \frac{\partial F_{A2}(j_{max})}{\partial B_{j-1/2}} \Delta B_{j-1/2} + \frac{\partial F_{A2}(j_{max})}{\partial (w_0)_{j-1/2}} \Delta (w_0)_{j-1/2} + \frac{\partial F_{A2}(j_{max})}{\partial (w_1)_j} \Delta (w_1)_j \right) = -F_{A2}(j_{max}) \\
 \sum_{j_{min}+1}^{j_{max}} \left( \frac{\partial F_{A3}(j_{max})}{\partial B_{j-1/2}} \Delta B_{j-1/2} + \frac{\partial F_{A3}(j_{max})}{\partial (w_0)_{j-1/2}} \Delta (w_0)_{j-1/2} + \frac{\partial F_{A3}(j_{max})}{\partial (w_1)_j} \Delta (w_1)_j \right) = -F_{A3}(j_{max}) \\
 \sum_{j_{min}+1}^{j_{max}} \left( \frac{\partial F_{A4}(j_{max})}{\partial B_{j-1/2}} \Delta B_{j-1/2} + \frac{\partial F_{A4}(j_{max})}{\partial (w_0)_{j-1/2}} \Delta (w_0)_{j-1/2} + \frac{\partial F_{A4}(j_{max})}{\partial (w_1)_j} \Delta (w_1)_j \right) = -F_{A4}(j_{max}),
 \end{array} \right.$$

where  $F_{A2}(j)$ ,  $F_{A3}(j)$ , and  $F_{A4}(j)$  are the left-hand sides of the Eqs. [A2], [A3], and [A4], respectively and the value of their derivatives is calculated numerically. This system of equations can be written in matrix form as:

$$\mathbf{A} \cdot \mathbf{x} = \mathbf{b}, \quad (\text{A9})$$

where  $\mathbf{A}$  is the matrix of the coefficients (the so-called Jacobian of the system), the raised dot denotes matrix multiplication, and  $\mathbf{x}$  and  $\mathbf{b}$  are the unknown corrections and the known right-hand sides (written as column vectors), respectively. They read:

$$\mathbf{A} = \begin{bmatrix}
 \frac{\partial F_{A2}(j_{min}+1)}{\partial B_{(j_{min}+1)-1/2}} & \dots & \frac{\partial F_{A2}(j_{min}+1)}{\partial B_{j-1/2}} & \frac{\partial F_{A2}(j_{min}+1)}{\partial (w_0)_{j-1/2}} & \frac{\partial F_{A2}(j_{min}+1)}{\partial (w_1)_j} & \dots & \frac{\partial F_{A2}(j_{min}+1)}{\partial (w_1)_{j_{max}}} \\
 \frac{\partial F_{A3}(j_{min}+1)}{\partial B_{(j_{min}+1)-1/2}} & \dots & \frac{\partial F_{A3}(j_{min}+1)}{\partial B_{j-1/2}} & \frac{\partial F_{A3}(j_{min}+1)}{\partial (w_0)_{j-1/2}} & \frac{\partial F_{A3}(j_{min}+1)}{\partial (w_1)_j} & \dots & \frac{\partial F_{A3}(j_{min}+1)}{\partial (w_1)_{j_{max}}} \\
 \frac{\partial F_{A4}(j_{min}+1)}{\partial B_{(j_{min}+1)-1/2}} & \dots & \frac{\partial F_{A4}(j_{min}+1)}{\partial B_{j-1/2}} & \frac{\partial F_{A4}(j_{min}+1)}{\partial (w_0)_{j-1/2}} & \frac{\partial F_{A4}(j_{min}+1)}{\partial (w_1)_j} & \dots & \frac{\partial F_{A4}(j_{min}+1)}{\partial (w_1)_{j_{max}}} \\
 \vdots & & \vdots & \vdots & \vdots & & \vdots \\
 \vdots & & \vdots & \vdots & \vdots & & \vdots \\
 \frac{\partial F_{A2}(j)}{\partial B_{(j_{min}+1)-1/2}} & \dots & \frac{\partial F_{A2}(j)}{\partial B_{j-1/2}} & \frac{\partial F_{A2}(j)}{\partial (w_0)_{j-1/2}} & \frac{\partial F_{A2}(j)}{\partial (w_1)_j} & \dots & \frac{\partial F_{A2}(j)}{\partial (w_1)_{j_{max}}} \\
 \frac{\partial F_{A3}(j)}{\partial B_{(j_{min}+1)-1/2}} & \dots & \frac{\partial F_{A3}(j)}{\partial B_{j-1/2}} & \frac{\partial F_{A3}(j)}{\partial (w_0)_{j-1/2}} & \frac{\partial F_{A3}(j)}{\partial (w_1)_j} & \dots & \frac{\partial F_{A3}(j)}{\partial (w_1)_{j_{max}}} \\
 \frac{\partial F_{A4}(j)}{\partial B_{(j_{min}+1)-1/2}} & \dots & \frac{\partial F_{A4}(j)}{\partial B_{j-1/2}} & \frac{\partial F_{A4}(j)}{\partial (w_0)_{j-1/2}} & \frac{\partial F_{A4}(j)}{\partial (w_1)_j} & \dots & \frac{\partial F_{A4}(j)}{\partial (w_1)_{j_{max}}} \\
 \vdots & & \vdots & \vdots & \vdots & & \vdots \\
 \vdots & & \vdots & \vdots & \vdots & & \vdots \\
 \frac{\partial F_{A2}(j_{max})}{\partial B_{(j_{min}+1)-1/2}} & \dots & \frac{\partial F_{A2}(j_{max})}{\partial B_{j-1/2}} & \frac{\partial F_{A2}(j_{max})}{\partial (w_0)_{j-1/2}} & \frac{\partial F_{A2}(j_{max})}{\partial (w_1)_j} & \dots & \frac{\partial F_{A2}(j_{max})}{\partial (w_1)_{j_{max}}} \\
 \frac{\partial F_{A3}(j_{max})}{\partial B_{(j_{min}+1)-1/2}} & \dots & \frac{\partial F_{A3}(j_{max})}{\partial B_{j-1/2}} & \frac{\partial F_{A3}(j_{max})}{\partial (w_0)_{j-1/2}} & \frac{\partial F_{A3}(j_{max})}{\partial (w_1)_j} & \dots & \frac{\partial F_{A3}(j_{max})}{\partial (w_1)_{j_{max}}} \\
 \frac{\partial F_{A4}(j_{max})}{\partial B_{(j_{min}+1)-1/2}} & \dots & \frac{\partial F_{A4}(j_{max})}{\partial B_{j-1/2}} & \frac{\partial F_{A4}(j_{max})}{\partial (w_0)_{j-1/2}} & \frac{\partial F_{A4}(j_{max})}{\partial (w_1)_j} & \dots & \frac{\partial F_{A4}(j_{max})}{\partial (w_1)_{j_{max}}}
 \end{bmatrix}$$



$$\mathbf{x} = \begin{bmatrix} \Delta B_{(j_{min}+1)-1/2} \\ \Delta(w_0)_{(j_{min}+1)-1/2} \\ \Delta(w_1)_{(j_{min}+1)} \\ \vdots \\ \Delta B_{j-1/2} \\ \Delta(w_0)_{j-1/2} \\ \Delta(w_1)_j \\ \vdots \\ \Delta B_{(j_{max})-1/2} \\ \Delta(w_0)_{(j_{max})-1/2} \\ \Delta(w_1)_{(j_{max})} \end{bmatrix} \quad \mathbf{b} = \begin{bmatrix} -F_{A2}(j_{min}+1) \\ -F_{A3}(j_{min}+1) \\ -F_{A4}(j_{min}+1) \\ \vdots \\ -F_{A2}(j) \\ -F_{A3}(j) \\ -F_{A4}(j) \\ \vdots \\ -F_{A2}(j_{max}) \\ -F_{A3}(j_{max}) \\ -F_{A4}(j_{max}) \end{bmatrix}.$$

Given the functional dependence of  $F_{A2}(j)$ ,  $F_{A3}(j)$ , and  $F_{A4}(j)$  from  $B_{j-1/2}$ ,  $(w_0)_{j-1/2}$ , and  $(w_1)_j$ , the matrix of coefficients  $\mathbf{A}$  is a so-called “band diagonal” matrix having nonzero elements only on the diagonal plus  $m_1$  ( $=6$  at most) elements immediately to the left of (or below) the diagonal and  $m_2$  ( $=4$  at most) elements immediately to the right (or above it). In other words, the elements of  $\mathbf{A}$  are equal to zero if either the column index  $h$  is greater than the row index  $k + m_2$  or the row index  $k$  is greater than the column index  $h + m_1$ .

In order to solve the system [A9] in an efficient way, minimizing the CPU time and the required storage space, we adopt a matrix inversion package based on a LU decomposition, where the matrix  $\mathbf{A}$  is stored and manipulated in a so-called “compact form”, in which only the non-zero elements are considered (see, e.g., Press et al. 1996, for details).

In addition, in order to increase the numerical accuracy, we use an iterative improvement of the solution  $\mathbf{x}$ . Specifically, we approximate  $\mathbf{x}$  with  $\mathbf{x}_0 + \delta\mathbf{x}_0$ , where  $\mathbf{x}_0$  is the solution of the system  $\mathbf{A} \cdot \mathbf{x} = \mathbf{b}$  and  $\delta\mathbf{x}_0$  – the first-order correction to  $\mathbf{x}_0$  – is the solution of the system  $\mathbf{A} \cdot \delta\mathbf{x} = (\mathbf{b} - \mathbf{A}\mathbf{x}_0)$  (see, e.g., Press et al. 1996, for details).

M.L.P. acknowledges financial support from the municipality of Padua through the prize *Padova Città delle Stelle*, and from the Bonino-Pulejo Foundation. We also acknowledge financial support from the PRIN-INAF 2009 “Supernovae Variety and Nucleosynthesis Yields”. We are grateful to the TriGrid VL project and the INAF-Astronomical Observatory of Padua for the use of computer facilities. Finally, we thank Stefano Benetti, Enrico Cappellaro, Paolo Mazzali, and Massimo Turatto for their useful comments.

## REFERENCES

- Alexander, D. R., & Ferguson, J. W. 1994, *ApJ*, 437, 879  
 Arnett, D. 1980, *ApJ*, 237, 541  
 Arnett, D. 1996, *Supernovae and Nucleosynthesis*, (Princeton: Princeton Univ. Press)  
 Astier, P., et al. 2006, *A&A*, 447, 31  
 Baklanov, P. V., Blinnikov, S. I., Pavlyuk, N. N. 2005, *Astronomy Letters*, 31, 429  
 Balberg, S., Zampieri, L., & Shapiro, S. L. 2000, *ApJ*, 541, 860  
 Baron, E., Nugent, P. E., Branch, D., Hauschildt, P. H. 2004, *ApJ*, 616, L91  
 Bersten, M. C., Benvenuto, O., Hamuy, M. 2011, *ApJ*, 729, 61  
 Blinnikov, S. I., & Popov, D. V. 1993, *A&A*, 274, 775  
 Blinnikov, S. I., Eastman, R., Bartunov, O. S., Popolitov, V. A., Woosley, S. E. 1998, *ApJ*, 496, 454  
 Cappellaro, E., & Turatto, M. 2000, in “The influence of binaries on stellar population studies”, Ed. D. Vanbeveren, (arXiv:astro-ph/0012455v1)  
 Cappellaro, E., et al. 2005, *A&A*, 430, 83  
 Catchpole, R. M., et al. 1987, *MNRAS*, 229, 15  
 Catchpole, R. M., et al. 1988, *MNRAS*, 231, 75  
 Chieffi, A., & Limongi, M. 2004, *ApJ*, 608, 405  
 Chieffi, A., Limongi, M., Straniero, O. 1998, *ApJ*, 502, 737  
 Chieffi, A., Domínguez, I., Höflich, P., Limongi, M., Straniero, O. 2003, *MNRAS*, 345, 111  
 Colpi, M., Shapiro, S. L., & Wasserman, I. 1996, *ApJ*, 470, 1075  
 Dessart, L., et al. 2008, *ApJ*, 675, 644  
 Dessart, L., Livne, E., Waldman, R. 2010, *MNRAS*, 408, 827  
 Duan, H., & Kneller, J. P. 2009, *J. Phys. G: Nucl. Part. Phys.*, 36, 113201  
 Eastman, R. G., Schmidt, B. P., Kirshner, R. 1996, *ApJ*, 466, 911  
 Elmhamdi, A., Chugai, N. N., Danziger, I. J. 2003, *A&A*, 404, 1077  
 Filippenko, A. V. 1997, *ARA&A*, 35, 309  
 Freedman, W. L., et al. 2009, *ApJ*, 704, 1036  
 Hamuy, M. 2003a, in Review for “Core Collapse of Massive Stars”, Ed. Fryer, Kluwer, Dordrecht  
 (arXiv:astro-ph/0301006v1)  
 Hamuy, M. 2003b, *ApJ*, 582, 905  
 Hamuy, M., & Pinto, P. A. 2002, *ApJ*, 566, L63  
 Hamuy, M., Suntzeff, N. B., Gonzales, R., Martin, G. 1988, *AJ*, 95, 63  
 Haugs, A., Rebel, H., Roth, M. 2003, *Rep. on Prog. in Phys.*, 66, 1145  
 Heger, A., Fryer, C. L., Woosley, S. E., Langer, N., Hartmann, D. H. 2003, *ApJ*, 591, 288  
 Herzig, K., El Eid, M. F., Fricke, K. J., Langer, N. 1990, *A&A*, 233, 462  
 Hicken, M. 2009, *ApJ*, 700, 1097  
 Kasen, D., & Woosley, S. E. 2009, *ApJ*, 703, 2205  
 Kirshner, R. P., & Kwan, J. 1974, *ApJ*, 193, 27  
 Inserra, C. et al. 2011, *MNRAS*, accepted (arXiv:1102.5468)  
 Iwamoto, K. et al. 2000, *ApJ*, 534, 660  
 Limongi, M., Straniero, O., & Chieffi, A. 2000, *ApJSS*, 129, 625  
 Limongi, M., & Chieffi, A. 2003, *ApJ*, 592, 404  
 Litvinova, I. Y., Nadezhin, D. K. 1983, *Ap&SS*, 89, 89  
 Litvinova, I. Y., Nadezhin, D. K. 1985, *SvAL*, 11, 145  
 Madau, P., Della Valle, M., & Panagia, N. 1998, *MNRAS*, 297, L17  
 Magee, N. H., et al. 1995, *ASP Conf. Ser.*, 78, 51  
 Mazzali, P. A. 2000, *A&A*, 363, 705  
 Mazzali, P. A., & Lucy, L. B. 1993, *A&A*, 279, 447  
 Mitchell, R. C., Baron, E., Branch, D., Hauschildt, P. H., Nugent, P. E., Lundqvist, P., Blinnikov, S., Pun, C. S. J. 2002, *ApJ*, 574, 293  
 Nadyozhin, D. K., 2003, *MNRAS*, 346, 97  
 Nobili, L., & Turolla, R. 1988, *ApJ*, 333, 248  
 Nobili, L., Turolla, R., & Zampieri, L. 1991, *ApJ*, 383, 250  
 Nugent, P., et al. 2006, *ApJ*, 645, 841  
 Olivares, E., et al. 2010, *ApJ*, 715, 833  
 Pagliaroli, G., Vissani, F., Coccia, E., Fulgione, W. 2009, *Phys. Rev. Lett.*, 103, 031102  
 Pastorello, A., et al. 2009, *MNRAS*, 394, 2266  
 Perlmutter, S., et al. 1999, *ApJ*, 517, 565  
 Phillips, M. M., Heathcote, S. R., Hamuy, M., Navarette, M. 1988, *AJ*, 95, 1087  
 Popov, D. V. 1993, *ApJ*, 414, 712

- Press, W. H., Teukolsky, S. A., Vetterling, W. T., & Flannery, B. P. 1996, *Numerical Recipes in FORTRAN 90* (Cambridge: Cambridge Univ. Press)
- Pumo, M. L., et al. 2009, *ApJ*, 705, L138
- Pumo, M. L., Zampieri L., Turatto, M. 2010, *Mem. S.A.It. Suppl.*, 14, 123
- Ratnatunga, K. U., & van den Bergh, S. 1989, *ApJ*, 343, 713
- Riess, A. G., et al. 1998, *AJ*, 116, 1009
- Shigeyama, T., & Nomoto, K. 1990, *ApJ*, 360, 242
- Shigeyama, T., Nomoto, K., Hashimoto, M. 1988, *A&A*, 196, 141
- Swartz, D. A., Wheeler, J. C., Harkness, R. P. 1991, *ApJ*, 374, 266
- Utrobin, V. P. 2004, *Astronomy Letters*, 30, 293
- Utrobin, V. P. 2007, *A&A*, 461, 233
- Utrobin, V. P., & Chugai, N. N. 2008, *A&A*, 491, 507
- Turatto, M., Benetti, S., & Pastorello, A. 2007, *AIPC*, 937, 187
- Wood-Vasey, W. M., et al. 2007, *ApJ*, 666, 694
- Woosley, S. E. 1988, *ApJ*, 330, 218
- Woosley, S. E., & Weaver, T. A. 1986, *ARA&A*, 24, 205
- Woosley, S. E., Pinto, P. A., & Hartmann, D. 1989, *ApJ*, 346, 395
- Young, T. R., 2004, *ApJ*, 617, 1233
- Zampieri, L. 2005, *ASPC*, 342, 358
- Zampieri, L. 2007, *AIPC*, 924, 358
- Zampieri, L., Miller, J. C., & Turolla, R. 1996, *MNRAS*, 281, 1183
- Zampieri, L., Colpi, M., Shapiro, S. L., & Wasserman, I. 1998, *ApJ*, 505, 876
- Zampieri, L., et al. 2003, *MNRAS*, 338, 711